JGR Space Physics

RESEARCH ARTICLE
10.1029/2022JA030619

A New Mechanism for Early-Time Plasmaspheric Refilling: The Role of Charge Exchange Reactions in the Transport of Energy and Mass Throughout the Ring Current—Plasmasphere System

Jianghuai Liu[1], Raluca Ilie[1], Joseph E. Borovsky[2], and Michael W. Liemohn[3]

[1]Department of Electrical and Computer Engineering, University of Illinois at Urbana-Champaign, Urbana, IL, USA, [2]Space Science Institute, Boulder, CO, USA, [3]Department of Climate and Space Science and Engineering, University of Michigan, Ann Arbor, MI, USA

Key Points:

- Ring current heavy ions are responsible for the production of over 50% of the cold H^+ population following a geomagnetic storm
- The density of H^+ produced via charge exchange reactions can be as high as ~10 times the local plasmaspheric density
- Cold H^+ production is limited by the abundance of heavy ions from the plasma sheet source; the exospheric structure does not play a role

Correspondence to:
J. Liu,
jliu115@illinois.edu

Citation:
Liu, J., Ilie, R., Borovsky, J. E., & Liemohn, M. W. (2022). A new mechanism for early-time plasmaspheric refilling: The role of charge exchange reactions in the transport of energy and mass throughout the ring current—plasmasphere system. *Journal of Geophysical Research: Space Physics*, *127*, e2022JA030619. https://doi.org/10.1029/2022JA030619

Received 5 MAY 2022
Accepted 22 SEP 2022
Corrected 21 OCT 2022

This article was corrected on 21 OCT 2022. See the end of the full text for details.

Author Contributions:
Conceptualization: Jianghuai Liu, Raluca Ilie
Data curation: Jianghuai Liu
Formal analysis: Jianghuai Liu, Raluca Ilie
Funding acquisition: Raluca Ilie
Investigation: Jianghuai Liu, Raluca Ilie
Methodology: Jianghuai Liu, Raluca Ilie
Project Administration: Raluca Ilie
Resources: Jianghuai Liu, Raluca Ilie

Abstract Cold H^+ produced via charge exchange reactions between ring current ions and exospheric neutral hydrogen constitutes an additional source of cold plasma that further contributes to the plasmasphere and affects the plasma dynamics in the Earth's magnetosphere system; however, its production and associated effects on the plasmasphere dynamics have not been fully assessed and quantified. In this study, we perform numerical simulations mimicking an idealized three-phase geomagnetic storm to investigate the role of heavy ion composition in the ring current (O^+ vs. N^+) and exospheric neutral hydrogen density in the production of cold H^+ via charge exchange reactions. It is found that ring current heavy ions produce more than 50% of the total cold H^+ via charge exchange reactions, and energetic N^+ is more efficient in producing cold H^+ via charge exchange reactions than O^+. Furthermore, the density structure of the cold H^+ is highly dependent on the mass of the parent ion; that is, cold H^+ deriving from charge exchange reactions involving energetic O^+ with neutral hydrogen, populates the lower L-shells, while cold H^+ deriving from charge exchange reactions involving energetic N^+ with neutral hydrogen populates the higher L-shells. In addition, the density of cold H^+ produced via charge exchange reactions involving N^+ can be peak at values up to one order of magnitude larger than the local plasmaspheric density, suggesting that solely considering the supply of cold plasma from the ionosphere to the plasmasphere can lead to a significant underestimation of plasmasphere density.

1. Introduction

The terrestrial magnetospheric environment comprises of plasma populations with a wide range of energy profiles, spanning from the sub-eV and eV particles of the ionosphere and plasmasphere, up to the ultra-relativistic energies of the radiation belts particles. These diverse plasma populations coexist, interact, and exchange energy via a multitude of collisional and wave-particle interactions (e.g., Liemohn, 2006; Yu et al., 2019). The detection of cold plasma populations is significantly impacted by spacecraft charging and secondary-electron contamination, which make reliable measurements of the cold ion populations and their analysis difficult (e.g., Delzanno et al., 2021; Genestreti et al., 2017; Gershman et al., 2017; Moore et al., 1997; Mozer et al., 2016). The main source of the magnetospheric cold plasma is the ionosphere (Andersson et al., 2004; Artemyev et al., 2020; Coley et al., 2003; Dandouras, 2021; Haaland et al., 2015), which can also contribute to the hot component of the magnetospheric plasma (Brambles et al., 2010; Chappell et al., 1987; Glocer et al., 2009; Huddleston et al., 2005; Welling, André, et al., 2015; Welling & Ridley, 2010; Winglee, 2000). There is growing evidence that supports the hypothesis that magnetospheric cold plasma populations play critical roles in several important processes that drive the dynamics of the region (Borovsky et al., 2013; Brambles et al., 2011; Delzanno et al., 2021; Ouellette et al., 2013; Trung et al., 2019; Welling, Jordanova, et al., 2015; Wiltberger et al., 2010; Winglee et al., 2002). As a result, understanding the origin, properties, drivers, and impacts of cold plasma is a key to fully understand the magnetosphere–ionosphere system.

While the cold-particle populations are sourcing a significant portion of the magnetospheric hot plasma, hot-particle populations can also become the source of cold plasma via charge exchange processes with regional neutral atoms (e.g., Borovsky et al., 2022). Due to the spatial overlap of the ring current with the Earth's neutral exosphere (Carruthers et al., 1976; Rairden et al., 1986), charge exchange processes between the low-energy exospheric neutral hydrogen atoms and the ring current ions, which allow for an energetic ion to pick up the

Software: Jianghuai Liu, Raluca Ilie
Supervision: Raluca Ilie
Validation: Jianghuai Liu, Raluca Ilie
Visualization: Jianghuai Liu, Raluca Ilie
Writing – original draft: Jianghuai Liu, Raluca Ilie
Writing – review & editing: Jianghuai Liu, Raluca Ilie, Joseph E. Borovsky, Michael W. Liemohn

orbital electron of a cold exospheric neutral hydrogen atom, lead to the formation of Energetic Neutral Atoms (ENAs) accompanied by low-energy H^+. Therefore, the charge exchange process not only represents an important loss mechanism for the ring current energy density (Ilie & Liemohn, 2016; Ilie et al., 2013; Kistler et al., 1989; Liemohn & Kozyra, 2003, 2005; Liemohn et al., 1999; Smith & Bewtra, 1978), but also leads to unstable hot-ion distributions in the ring current region (Cornwall, 1977; Thomsen et al., 2011, 2017), and may also shorten the early-phase of the plasmaspheric refilling (Denton & Borovsky, 2014; Obana et al., 2010; Sojka & Wrenn, 1985; Su et al., 2001). While the density of exospheric neutral hydrogen decreases exponentially with increasing distance away from the Earth (e.g., Borovsky et al., 2022; Chamberlain, 1963; Ilie et al., 2013), the details of cold H^+ production via charge exchange depend on the energy profile, equatorial temperature distribution, convection drift pattern, and ion composition of the hot plasma. Due to the different charge exchange cross sections for reactions involving various ring current species with neutral hydrogen, changes in the regional ion composition can lead to changes in the cold H^+ population formed via the charge exchange interaction. Both numerical simulations and in situ measurements indicate that the ring current ion composition changes with the geomagnetic activity, and heavy ions (N^+ and O^+) can contribute significantly to the ring current number density during storm time (Fu et al., 2001; Hultqvist, 1979, 1982; Ilie et al., 2015; James et al., 2021; Kistler & Mouikis, 2016; Kozyra et al., 2002; Lee et al., 2021; Orsini, 2004; Zhao et al., 2015).

In this study, we assess the role of heavy ion composition of the ring current (and plasma sheet) in the production of cold H^+ via charge-exchange reactions. We present qualitative and quantitative estimations of the generation and time-evolution of these cold H^+, with a special focus on those produced by the ring current N^+ and O^+ ions, based on numerical simulations using the Hot Electron-Ion Drift Integrator (HEIDI) model. In addition, the associated effects on the plasmaspheric refilling are also discussed.

2. Methodology

The HEIDI model is an inner magnetosphere kinetic drift model that solves the time-dependent, gyration- and bounce-averaged Boltzmann equation for the equatorial phase-space distribution function $F(t, \mathbf{r}_0, \mathbf{v}_0)$ of five ring current species (e^-, H^+, He^+, N^+, O^+). The computational domain is defined by the surface of magnetic field minima between 2 and 6.5 Earth radii, discretized uniformly both in the radial and azimuthal directions, and is capable of handling arbitrary electric and magnetic fields. The bounce-averaged kinetic equation solved is (Ilie et al., 2012; Liemohn et al., 2004):

$$\frac{\partial F}{\partial t}+\frac{1}{R_0^2}\frac{\partial}{\partial R_0}\left(R_0^2\left\langle\frac{dR_0}{dt}\right\rangle F\right)+\frac{\partial}{\partial \phi_0}\left(\left\langle\frac{d\phi_0}{dt}\right\rangle F\right)+\frac{1}{\sqrt{W}}\frac{\partial}{\partial W}\left(\sqrt{W}\left\langle\frac{dW}{dt}\right\rangle F\right)+\frac{1}{h(\mu_0)\,\mu_0}\frac{\partial}{\partial \mu_0}\left(h(\mu_0)\,\mu_0\left\langle\frac{d\mu_0}{dt}\right\rangle F\right)=\left\langle\frac{\delta F}{\delta t}\right\rangle_{collision}+\left\langle\frac{\delta F}{\delta t}\right\rangle_{source} \quad (1)$$

Equation 1 describes the time-evolution of the phase-space distribution function at a certain location ($\mathbf{r}_0$, $\mathbf{v}_0$) within the configuration-velocity space, under the effect of drifts, energization, pitch-angle scattering, and various loss mechanisms. Ring current losses include Coulomb collisions, charge exchange reactions with the hydrogen exosphere, and precipitative losses to the upper atmosphere, all considering full pitch angle distributions. The five independent variables that constitute the equatorial phase-space distribution function $F(t, \mathbf{r}_0, \mathbf{v}_0)$ are time t, radial distance on the magnetic equatorial plane R_0, azimuth ϕ_0, kinetic energy W, and the cosine of the equatorial pitch angle of each species $\mu_0 = \cos(\alpha_0)$. The size of the numerical grid was carefully determined to resolve the features of interest, maintain numerical stability and accuracy, but also to optimize the run-time of the simulation. The grid used in each mutually independent phase-space variable is as follows: 20s time step; 19 equally spaced radial grid points distributed from $2R_E$ to $6.5R_E$ geocentric distance ($\Delta R = 0.25R_E$); 24 equally spaced grid points in local time around the Earth $\left(\Delta\phi = \frac{\pi}{12} = 1\text{MLT}\right)$; 42 geometrically spaced energy grid points from 10 eV to 400 keV, with the geometric factor of 1.26; and 71 equatorial pitch angle grid points from 90° to 0°, which corresponds to 0 to 1 in μ_0 and is more refined within loss cone angle. To calculate the bounce-averaged coefficients, HEIDI traces each individual field line whose equatorial intersection lies in the computation domain, and employs a field-aligned grid that discretizes each field line (set to 101 points along the field line for this study, as described in Ilie et al., 2012), along which the numerical integration is performed. The source term on the right hand side of Equation 1 is represented by the plasma sheet conditions on the nightside outer boundary of the simulation domain, using plasma sheet particle fluxes as the outer boundary condition.

The HEIDI model considers the loss of individual ring current ion species via charge exchange reactions with the neutral hydrogen exosphere, as described below:

$$H^+_{hot} + H \rightarrow H^+_{cold} + H \tag{2}$$

$$He^+_{hot} + H \rightarrow H^+_{cold} + He \tag{3}$$

$$O^+_{hot} + H \rightarrow H^+_{cold} + O \tag{4}$$

$$N^+_{hot} + H \rightarrow H^+_{cold} + N \tag{5}$$

where the H^+_{cold} on the right hand side of each reaction denotes the cold protons produced via charge-exchange reactions between neutral hydrogen and ring current ions. At every time step, the charge exchange loss is reflected on the velocity distribution function $F_{X^+}(t, R_0, \phi_0, W, \mu_0)$, where $X^+ \in \{H^+, He^+, O^+, N^+\}$, as:

$$F_{X^+(after)}(t, R_0, \phi_0, W, \mu_0) = F_{X^+(before)}(t, R_0, \phi_0, W, \mu_0) \cdot \eta_{X^+(CE)}(R_0, \phi_0, W, \mu_0) \tag{6}$$

where $F_{X^+(before)}(t, R_0, \phi_0, W, \mu_0)$ and $F_{X^+(after)}(t, R_0, \phi_0, W, \mu_0)$ represent the distribution function of ion X^+ before and after the charge exchange reaction took place, respectively. Furthermore, the term $\eta_{X^+(CE)}(R_0, \phi_0, W, \mu_0)$ in Equation 6 represents the local charge exchange loss factor of ion species X^+, calculated via:

$$\eta_{X^+(CE)}(R_0, \phi_0, W, \mu_0) = \exp\left[-\sigma_{X^+}(W)\upsilon_{X^+}(W)\langle n_H\rangle(R_0, \phi_0, \mu_0)\Delta t\right] \tag{7}$$

where $\sigma_{X^+}(W)$ denotes the charge exchange cross section between species X^+ and exospheric neutral hydrogen (as a function of the kinetic energy W of the parent hot ion), $\upsilon_{X^+}(W)$ is the speed of X^+, Δt is the timestep, and $\langle n_H\rangle(R_0, \phi_0, \mu_0)$ is the bounce-averaged neutral hydrogen density. Because the exosphere models are time independent, the local charge exchange loss factor $\eta_{X^+(CE)}(R_0, \phi_0, W, \mu_0)$ is constant throughout the simulation.

The density distribution of the ring current species X^+ before and after the charge exchange process is obtained by evaluating the zeroth-order velocity moment of $F_{X^+(before)}$ and $F_{X^+(after)}$, respectively. The density of cold H^+ resulting from X^+ species, considering the contribution from the parent energetic ions of all energies and equatorial pitch-angles, is evaluated as:

$$\begin{aligned} n_{H^+_{cold}(X^+)}(t, R_0, \phi_0) &= n_{X^+(before)}(t, R_0, \phi_0) - n_{X^+(after)}(t, R_0, \phi_0) \\ &= \sum_k \sum_l F_{X^+(before)}(t, R_0, \phi_0, W_k, \mu_{0l})\left[1 - \eta_{X^+(CE)}(R_0, \phi_0, W_k, \mu_{0l})\right] W_k \mu_{0l} \end{aligned} \tag{8}$$

where k and l denote the discrete energy and equatorial pitch-angle indexes of the parent species X^+, respectively. The production of cold H^+ at each time step is accumulated, and the total density is obtained as the sum of the cold H^+ produced via charged exchange by all ring current ion species, as shown in Equation 9.

$$n_{H^+_{cold}(total)} = n_{H^+_{cold}(H^+)} + n_{H^+_{cold}(He^+)} + n_{H^+_{cold}(O^+)} + n_{H^+_{cold}(N^+)} \tag{9}$$

The cold H^+ are assumed to be neither interacting with each other, nor participating in Coulomb interactions. The four $n_{H^+_{cold}}$ terms on the right hand side of Equation 9 denote the cold H^+ density resulted from each of the four ring current ion species (e.g., $n_{H^+_{cold}(O^+)}$ represents the cold H^+ density produced via charge exchange reactions of ring current O^+ with neutral exospheric hydrogen).

3. Simulation Setup

We investigated the effects of plasma composition on the generation and evolution of the cold H^+ population produced via charge exchange reactions with ring current ions, assuming idealized storm-like conditions and two neutral hydrogen exosphere models. In this study, we employed two typical exosphere neutral hydrogen models: (a) the spherically symmetric Rairden et al. (1986) model obtained via fitting the radial density profile with measurements of exospheric atomic hydrogen obtained from the ultraviolet imaging photometer carried on the high-altitude Dynamics Explorer 1 satellite (DE 1), and (b) the Hodges (1994) model obtained via 3D spherical harmonic expansion, which allows for asymmetry in the neutral hydrogen density distribution both on the dawn-dusk and day-night meridian. Several other exosphere density models exist (e.g., Bailey & Gruntman, 2011,

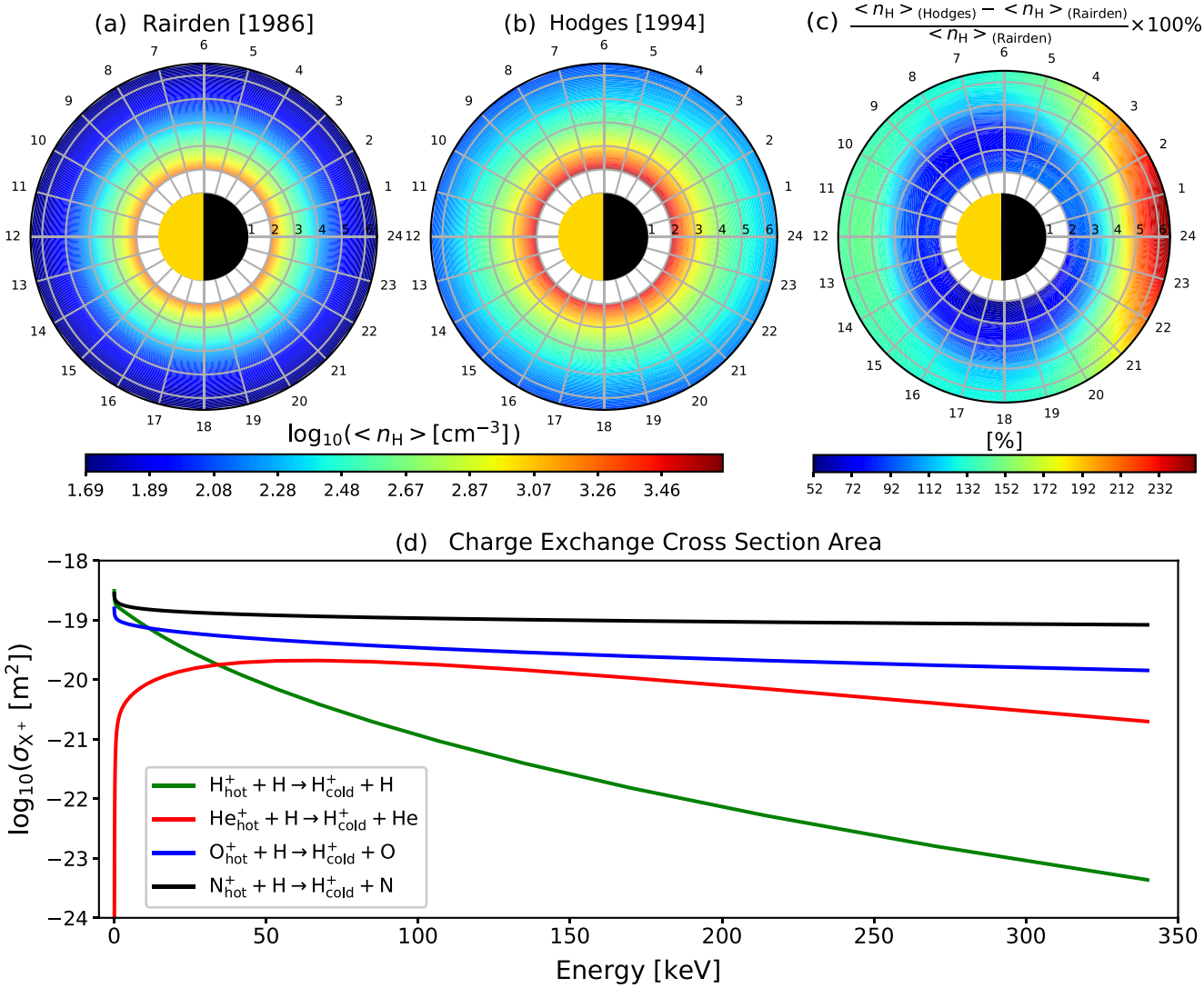

Figure 1. (a, b) Bounce-averaged neutral hydrogen density (on log scale) imposed to energetic ions with equatorial pitch-angle of 60°, using Rairden et al. (1986) model and Hodges (1994) model, respectively; (c) Percentage difference of the bounce-averaged exospheric neutral hydrogen density between the Rairden et al. (1986) model and Hodges (1994) model; (d) Charge exchange cross section versus energy for reactions between energetic ions and the exospheric neutral hydrogen (see the plot label).

2013; Zoennchen et al., 2011, 2015, 2022) and are included in the HEIDI model (Ilie et al., 2013); however, the formalism is based on the spherical harmonic expansion described in Hodges (1994), with the main difference that the expansion coefficients are either truncated or simplified. In the HEIDI model, the bounce-averaged neutral hydrogen density $\langle n_H \rangle$ is used to obtain the charge-exchange loss rate, as expressed in Equation 7. Panels (a) and (b) in Figure 1 show the bounce-averaged neutral hydrogen density (in log scale) imposed for energetic ions with an equatorial pitch-angle of 60°, using the Rairden et al. (1986) model and Hodges (1994) model, respectively. The pitch-angle of 60° is selected as example because it represents the set of energetic ions that travel further along the field line. The neutral hydrogen density predicted by both exosphere models decreases exponentially toward larger L-shells, and while the Rairden et al. (1986) model possesses spherical symmetry, the Hodges (1994) model does not. To highlight these differences, panel (c) in Figure 1 shows the percentage difference between the neutral densities predicted by the two models, indicating that the Hodges (1994) model predicts notably higher densities than that of the Rairden et al. (1986) model, with a significant intensification over the nightside. Specifically, the bounce-averaged neutral density of the Hodges (1994) model increases over 200% from the Rairden et al. (1986) model on the nightside for L > 4, while only 150% on the dayside.

The probability of occurrence of charge exchange reactions between ring current ions and exospheric neutral hydrogen depends on the energy of the incident energetic particles, the ambient exospheric neutral density, and the charge exchange cross section. The energy profile of the charge exchange cross section (in log scale) is shown in panel (d) of Figure 1 (Phaneuf et al., 1987). The weighted average charge exchange cross section of neutral hydrogen with energetic H^+, O^+, and N^+ over all energies are $\sim 7 \times 10^{-21}$, $\sim 3 \times 10^{-20}$, and $\sim 1.0 \times 10^{-19}$ m^{-2}, respectively. These differences in the charge exchange cross sections for different ion species with neutral hydrogen are due to the different ionization potentials of each species (Rapp & Francis, 1962). Please note that the average charge exchange cross sections of both N^+ and O^+ with the cold neutral hydrogen are notably higher than that of H^+; the cross section for the reaction involving N^+ is $\sim$15 times larger than the cross section for the reaction involving H^+, while the cross section for the reaction involving O^+ is $\sim$4 times larger than the cross section for the reaction involving H^+. This implies that energetic heavy ions are able to produce cold H^+ via charge exchange reactions with ambient neutral hydrogen more effectively compared with energetic H^+ on average, given the same local neutral density and energy distribution of parent ions. In addition, there are differences between the charge exchange cross section for reactions involving N^+ versus O^+ and neutral hydrogen over the entire energy range; the cross section for the charge exchange reaction involving N^+ is on average 3.5 times larger than cross section for the charge exchange reaction involving O^+, which implies that the specific composition of energetic heavy ions (O^+ vs. N^+) affects the amount of cold H^+ produced via charge exchange reactions in the inner magnetosphere. In this study, we focus on the production and evolution of cold H^+ produced via charge exchange involving different energetic heavy ions in the inner magnetosphere.

Numerical simulations are performed using a set of idealized parameters, designed to mimic a three-phase geomagnetic storm that lasts for 72 hr, with a distinguishable quiet phase (the first 24 hr), main phase, and recovery phase (the last 24 hr). The variations of the Kp index and nightside boundary total ion density are illustrated in panel (a) of both Figure 2 and Figure 3. Specifically, the Kp index and total ions density on the nightside boundary are set to 1 and 2 cm^{-3} during both the quiet phase and recovery phase, and become 6 and 6 cm^{-3} in the main phase, respectively. The simulation transits from the quiet phase into the main phase in 3 hr from $T = 24$ to $T = 27$ hr, during which both the Kp index and the total plasma sheet density n_i on the outer boundary increase linearly to the main phase value, and transits from the main phase into the recovery phase in 3 hr from $T = 51$ to $T = 54$ hr, during which the Kp index and total ion density n_i on the outer boundary drop linearly to the quiet phase values. The ring current ion composition is set up by splitting the total ion density n_i on the outer boundary into H^+, He^+ and heavy ions ($O^+ + N^+$), via the Kp- and Ap-dependent statistical relationships derived by Young et al. (1982). The convection electric field is provided by the Kp-driven Volland-Stern's convection electric field model (Stern, 1975; Volland, 1973); and the dipolar magnetic field is strictly imposed across the computation domain throughout the entire simulation. In this study, we performed the three-phase storm simulation under two independent cases of heavy ions composition: one where all heavy ions on the outer boundary are assumed to be O^+, and the other where all heavy ions are assumed to be N^+. The simulation results are discussed in Section 4.

4. Results and Discussion

The simulation results are presented and discussed in this section: Section 4.1 explores the formation and evolution of the charge-exchange byproduct cold H^+ from the energetic heavy ions, with a primary focus on the storm phase and recovery phase, along with an investigation on the percentage contribution of energetic heavy ions to the cold H^+ over the total ring current ions; Section 4.2 compares the density of the byproduct cold H^+ via charge exchange with an activity dependent plasmasphere model, and discusses the potential effects of the byproduct cold H^+ on the dynamics of the plasmasphere.

4.1. Cold H^+ Production via Charge Exchange

Energetic heavy ions play a critical role in the production of the cold H^+ via charge exchange reactions, considering their notably higher average charge exchange cross sections compared with energetic H^+ between neutral hydrogen, as showed in panel (d) of Figure 1 and discussed in Section 3. We first examine the production of cold H^+ that resulted from the charge exchange of O^+ and N^+ ions with exospheric neutral hydrogen using the Rairden et al. (1986) exospheric density model, and assuming that the heavy ions injected on the nightside boundary are either 100% O^+ or 100% N^+, respectively. These assumptions are designed to highlight the role of plasma sheet heavy ion composition in the production of cold H^+. Note that most previous studies considered O^+ the only

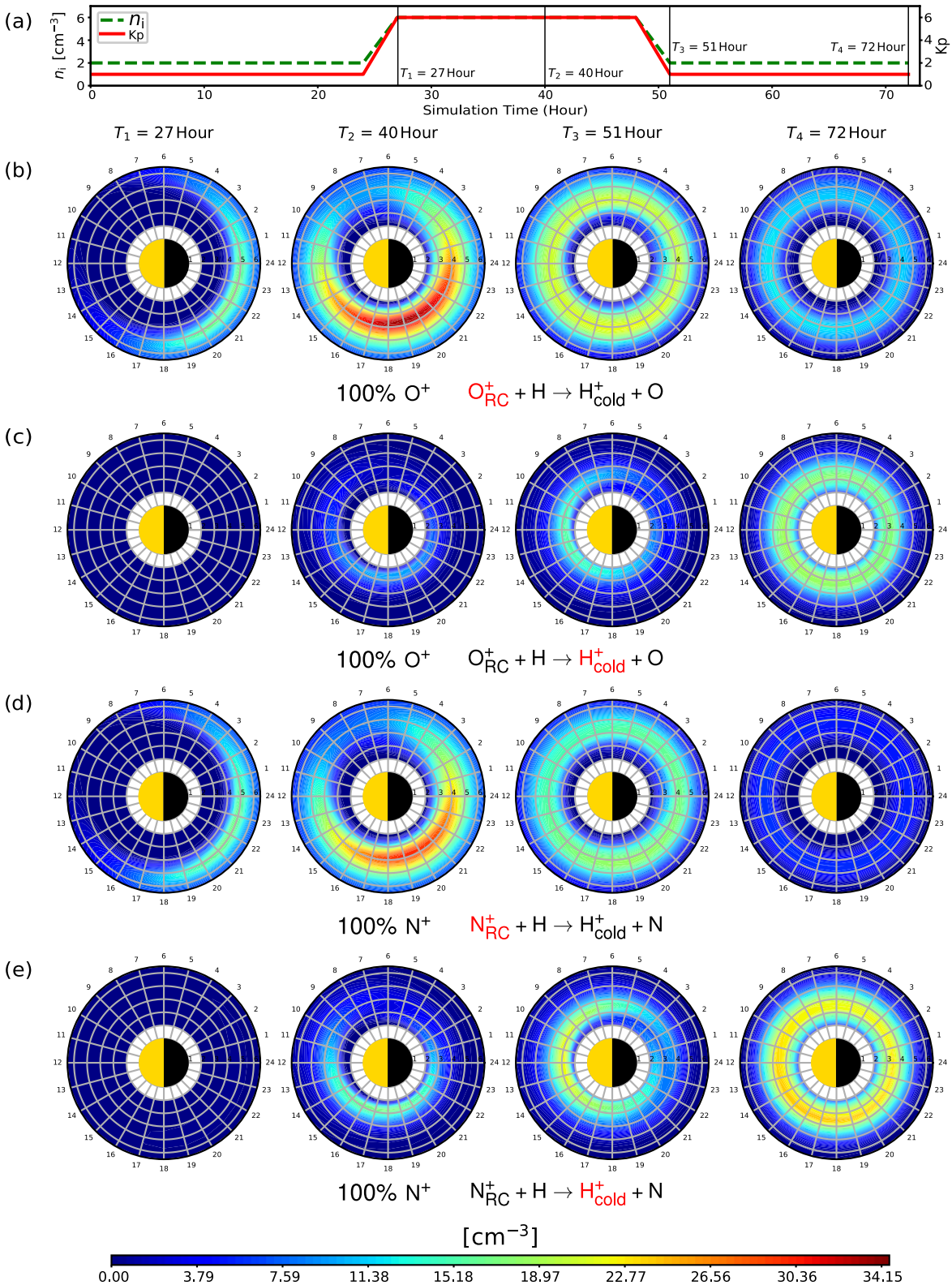

Figure 2. (a) Evolutionary tracks of the input parameters for the idealized storm simulations showing the Kp index (right *y*-axis, red line) and plasma sheet density on the nightside outer boundary (left *y*-axis, green line); (b–e) Plots showing the evolution of ring current heavy ions density and the associated charge-exchange byproduct cold H^+ at the four time instances, using the symmetric Rairden et al. (1986) model; (b, d) Ring current heavy ions density, assuming 100% O^+ and 100% N^+; (c, e) Charge-exchange byproduct cold H^+ density by the energetic heavy ions, assuming 100% O^+ and 100% N^+.

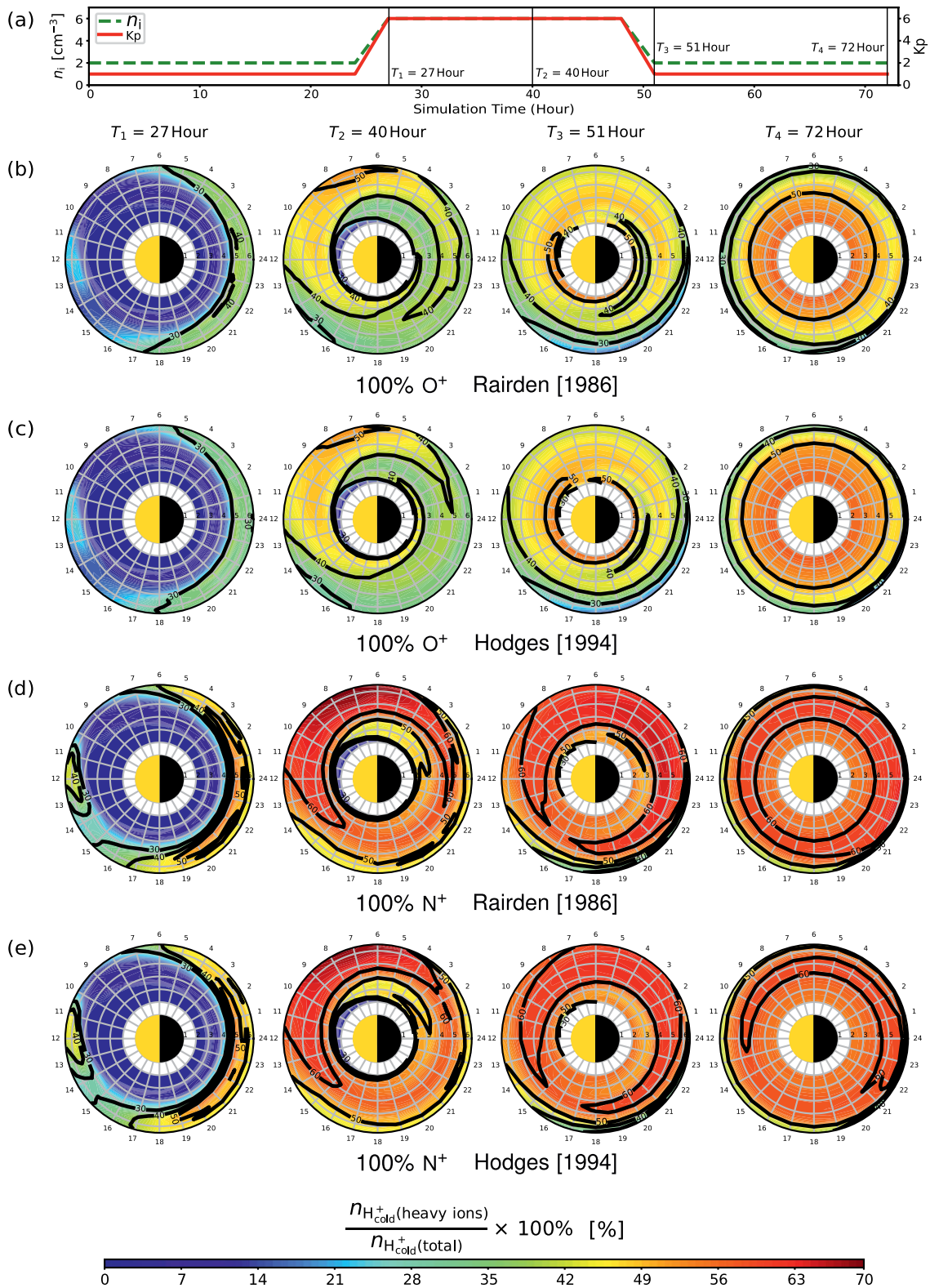

Figure 3. (a) Evolutionary tracks of the input parameters for the idealized storm simulations showing the Kp index (right *y*-axis, red line) and plasma sheet density on the nightside outer boundary (left *y*-axis, green line); (b–e) Plots showing the evolution of the cold H^+ density ratio (in %) between byproduct of the ring current heavy ions, and byproduct of the total ring current ions; (b, c) 100% O^+ using Rairden et al. (1986) model and Hodges (1994) model; (d, e) 100% N^+ using Rairden et al. (1986) model and Hodges (1994) model.

heavy ion participating the ring current dynamics, and this corresponds to our case of 100% O^+. Figure 2 shows the comparison between the ring current heavy ion densities and the associated cold H^+ resulting from the corresponding charge-exchange reactions, extracted at four times within the numerical simulation ($T_1 = 27$, $T_2 = 40$, $T_3 = 51$, and $T_4 = 72$ hr) indicated in panel (a). The following rows show the density of O^+ (row (b)) and N^+ (row (d)), and the associated cold H^+ (rows (c), (e)), as indicated by the highlighted red text at the bottom of each row.

At the beginning of the main phase ($T_1 = 27$ hr, the leftmost column), when both the convection strength and the flux on the nightside outer boundary are enhanced, we observe an increase in both O^+ and N^+ densities on the nightside centered on L = 5 shell, as freshly injected particles are drifting westward while convecting into the lower L-shells (see leftmost column of rows (b) and (d)). During this time, there is no significant production of cold H^+, which implies that the effects of charge-exchange reactions are not significant. This is due to the relatively low ring current ion densities, as well as to the fact that the peak density occurs at higher L-shells where the exospheric neutral density is low.

At $T_2 = 40$ hr during the storm main phase, we observe an enhancement in O^+ and N^+ densities in the evening sector (18 MLT—0 MLT quadrant) between L = 3 and L = 5 shells, mostly due to the continuous supply of particles from the nightside boundary and strong Sunward convection. At this time, cold H^+ is being produced and accumulated close to the model inner boundary across the duskside around L = 2.5 shell (see rows (c) and (e)). This is due to the fact that the neutral density is exponentially decreasing with distance away from the Earth, therefore the charge exchange reaction is most effective at low radial distances. In addition, the cold H^+ generated at higher L-shells (closer to the peak of ring current) are also drifting westward while convecting Earthward, leading to an accumulation of cold H^+ at lower L-shells.

At $T_3 = 51$ hr, which corresponds to the start of the recovery phase, the topology of the ring current becomes more symmetric. As energetic O^+ and N^+ drift around the simulation domain, they continue to undergo charge exchange reactions with the local exospheric neutral hydrogen, especially at lower L-shells where the density of neutral hydrogen is high. Therefore, we observe a fast accumulation of cold H^+ accompanied by a faster decay of both O^+ and N^+ density at low L-shells. We observe that at the end of the simulation ($T_4 = 72$ hr), the charge exchange reactions led to a significant loss of energetic O^+ and N^+ from the ring current (see rows (b) and (d)). On the other hand, this ring current decay is associated with a significant production and accumulation of cold H^+ within L = 4 (rows (c) and (e)). The radial density profile of both the total energetic ions and the associated charge-exchange byproduct cold H^+ along MLT = 0 (midnight), captured at the end of the simulation ($T_4 = 72$ hr), are illustrated in panels (a) and (b) of Figure 4. It shows that the ring current ion density peaks between L = 4 and L = 4.5, while the associated byproduct cold H^+ density peaks around L = 3.5 (solid red and green) at the end of the simulation.

The evolution of the cold H^+ population associated with energetic O^+ and N^+ over the four time instances illustrated above, suggests that the production and topology of the cold ion population are closely controlled by the composition of ion plasma sheet along with the magnetospheric convection. The ion plasma sheet provides energetic ion populations that can be converted into the cold populations via charge exchange reactions, and the magnetospheric convection further transports the hot ion populations and drives them into lower L-shells where the exospheric neutral density is high. Therefore, it is the collective and accumulative effect of both ion plasma sheet composition and magnetospheric convection that determines the abundance and topology of the cold populations associated with the ring current energetic ions.

Although energetic ring current O^+ and N^+ possess similar qualitative behaviors across the four time instances, significant quantitative differences exist. The energetic N^+ decays notably faster than O^+ during the recovery phase, as reflected by the density of O^+ and N^+ showed in rows (b) and (d) of Figure 2. Those differences are also highlighted by the radial density profiles represented by the (either solid or dashed) red versus green curves in panel (a) of Figure 4. The density of cold H^+ produced via charge exchange from N^+ with neutral hydrogen is notably higher than that produced in reactions involving O^+. This is due to the fact that the ring current N^+ undergoes more efficient charge-exchange loss than O^+ does, and has a shorter average ring current lifetime, primarily due to the difference in charge exchange cross sections as showed in Figure 1. The charge exchange cross section of hot N^+ with exospheric hydrogen is larger than that of O^+ across the entire considered energy range, inferring that the probability of energetic N^+ undergoing charge exchange reactions with the local cold neutral hydrogen is greater than that of energetic O^+, given the same local density of cold neutral hydrogen. As a result, energetic N^+

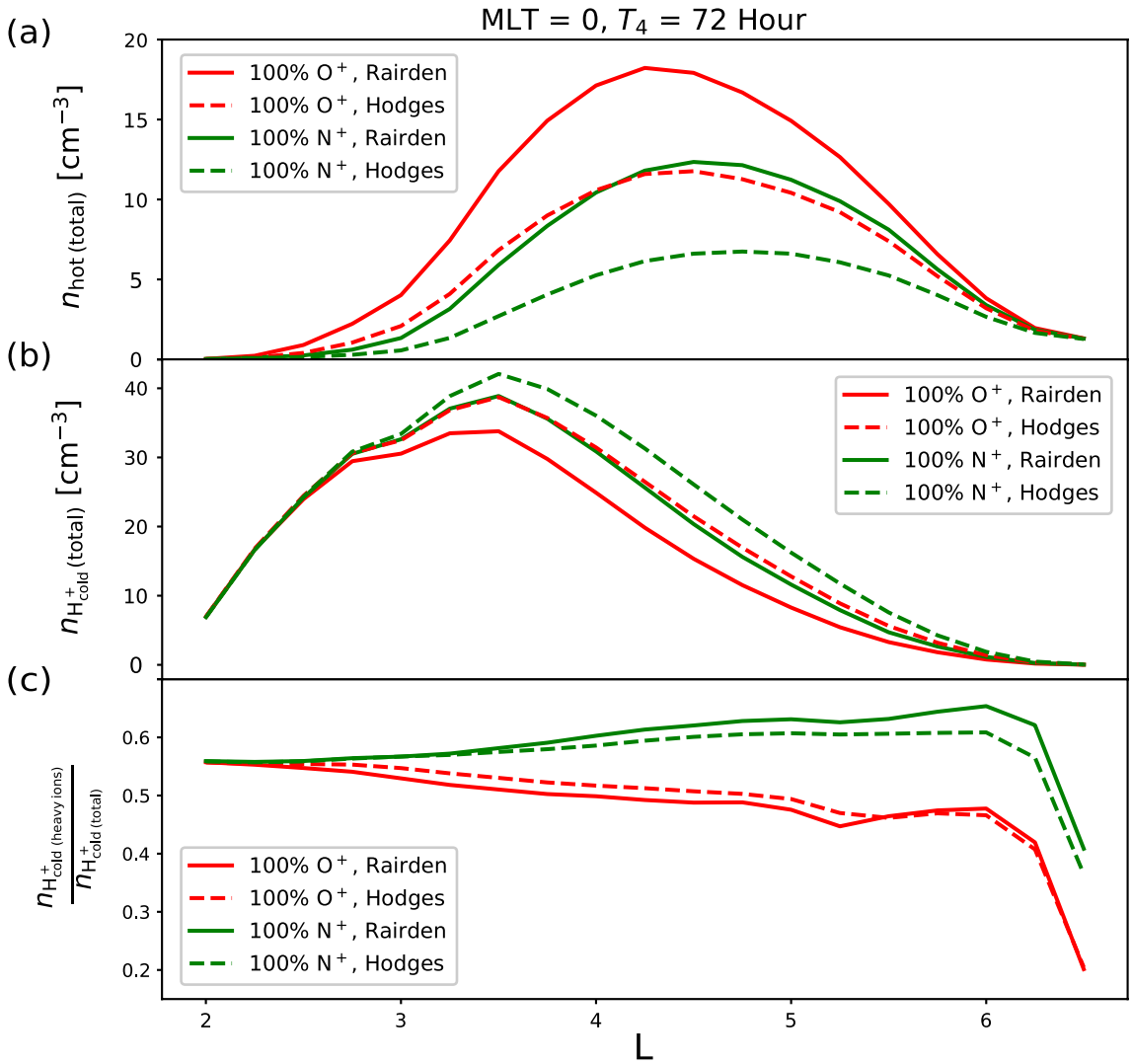

Figure 4. (a–c) Comparisons of radial profiles along MLT = 0 at the end of the simulation (T_4 = 72 hr), between the two different heavy ions compositions of 100% O^+ (red) and 100% N^+ (green), using Rairden et al. (1986) model (solid) and Hodges (1994) model (dashed); (a) The radial density profile of the total energetic ions; (b) The radial density profile of the charge-exchange byproduct cold H^+ resulting from all energetic ions; (c) The radial profile of the cold H^+ contribution from the energetic heavy ions.

is more efficient in producing cold H^+. The exosphere density also plays a role on the decay rate of the energetic ions, as inferred by the difference between solid and dashed curves of the same color in panels (a) and (b) of Figure 4.

Next, we perform a quantitative assessment of the contribution of energetic O^+ and N^+ to the local production of cold H^+ generated by the charge exchange reactions between the total ring current ions and neutral exosphere, for the two exospheric models described above. Figure 3 shows the fraction of $\frac{H^+_{cold(heavy\,ions)}}{H^+_{cold(total)}}$ (expressed in percentage) at the same four time moments discussed in Section 4.1. The black lines represent different contour levels of the fraction $\frac{H^+_{cold(heavy\,ions)}}{H^+_{cold(total)}}$, where $H^+_{cold(heavy\,ions)}$ denotes the cold H^+ derived from the charge exchange process involving a particular ring current heavy ion species (either O^+ or N^+) as indicated under the label of each row, along with the background exospheric neutral hydrogen model.

The contributions of cold H^+ associated with energetic O^+ and N^+ display distinct radial dependency, both qualitatively and quantitatively. At the end of the storm main phase (T_3 = 51 hr, the third column from the left), the

contribution of energetic O^+ to the production of cold H^+ is less than 50% over the majority of the simulation domain, independent on the exosphere model employed, as shown by the region outside of the 50% contribution contour in the third column from the left of rows (b) and (c); on the other hand, over 60% of cold H^+ is produced by charge exchange reactions of energetic N^+ with exospheric neutral hydrogen. This can be seen over a large region for L > 3 shell, independent of the exosphere model used, as shown by the region enclosed by the 60% contribution contour in the third column from the left of rows (d) and (e). At T_4 = 72 hr, the difference in cold H^+ contribution of O^+ or N^+ charge exchange reactions is significant; the contribution of cold H^+ produced from energetic O^+ via charge exchange reactions to the total cold H^+ population increases with decreasing distance from the Earth, with the 50% contribution contour centered at L = 4 for the simulation using the Rairden et al. (1986), whereas the same contour moves $1R_E$ outward for the simulation based on the Hodges (1994) exosphere model; in contrast, the contribution of the cold H^+ associated with energetic N^+ to the total cold H^+ population increases with increasing distance from the Earth, independent of the ambient exospheric neutral density distribution, as shown in the fourth column from the left of rows (d) and (e). The midnight (MLT = 0) radial profile of the cold H^+ contribution of both energetic O^+ and N^+ charge exchange reactions with the neutral exosphere is presented in panel (c) of Figure 4. These simulations results suggest cold H^+ produced via charge exchange reactions with ring current O^+ is produced at lower L-shells, whereas production via charge exchange reactions involving energetic N^+ is more efficient at larger L-shells (red curves vs. green curves). These differences imply that energetic O^+ ions have longer lifetimes and are more likely to convect into lower L-shells before they are lost via charge exchange; on the other hand, due to the high charge exchange cross section, energetic N^+ have shorter lifetimes and are lost via charge exchange reaction significantly faster, prohibiting their convection deeper into the inner magnetosphere. Furthermore, the radial dependency of cold H^+ production via either O^+ or N^+ charge exchange reactions is independent of the exospheric neutral hydrogen density, as seen in panel (c) of Figure 4.

The differences between the exospheric hydrogen densities predicted by the Rairden et al. (1986) and the Hodges (1994) models vary from ∼135% to ∼250% for L ≥ 3.5 (see Figure 1). However, at the end of the recovery phase (T_4 = 72 hr), this significant difference in neutral hydrogen density is only responsible for 1% change at best in the production of cold H^+, both for reactions involving O^+ and N^+. For instance, the average contribution of energetic O^+ to the production of cold H^+ increases from 47.7% to 49.2%, with an increase in the peak production fraction from 56.9% to 57.4%, as the exosphere model changes from the Rairden et al. (1986) to the Hodges (1994) model; however, the contribution of energetic N^+ to the production of cold H^+ is increasing by about 10% on average, as compared with the contribution of energetic O^+ for the same exospheric density distribution. Therefore, the production of cold H^+ is primarily determined by the plasma sheet composition, rather than the neutral exosphere density.

4.2. The Contribution of Cold H^+ to the Plasmasphere

Due to the spatial overlap between the plasmasphere and the ring current, the generation of cold H^+ via charge exchange can also affect the dynamics of the plasmasphere. To investigate these effects, we adopted the activity-dependent Dynamic Global Core Plasma Model (DGCPM) (Ober et al., 1997), included in the HEIDI model (Ilie et al., 2012; Liemohn et al., 2005). DGCPM simulates the evolution of the low-energy plasma density by solving the mass continuity equation along convecting magnetic flux tubes for the total cold ion content. The plasmaspheric density distribution (in log scale) at four different time moments (T_0 = 24, T_3 = 51, T_3' = 58, and T_4 = 72 hr) are shown in row (b) of Figure 5. Please note that T_3 and T_4 are the same with the ones discussed in Section 4.1, while T_0 and T_3' are two additional timestamps introduced in this section, as they are relevant in the context of the plasmasphere dynamics. At the end of the quiet phase (T_0 = 24 hr, the leftmost column), the distributions of plasmaspheric cold density is approximately symmetric around the Earth, with a slight dusk bulge. At the end of the storm main phase (T_3 = 51 hr, the second column from the left), the plasmasphere has been significantly eroded, with the plasmaspheric drainage plume extending from the afternoon sector (12 MLT—18 MLT quadrant), and a well-defined nightside plasmapause density gradient. The plasmasphere gradually refills during the recovery phase (51 hr < T < 72 hr), with the drainage plume rotating eastward and the cold plasma density recovers.

The cold H^+ population produced via charge exchange reactions between ring current ions and neutral exospheric hydrogen also contributes to the overall plasmaspheric cold plasma density, therefore further affects its dynamics. Figure 6 shows the comparison of cold plasma as 10 cm^{-3} (red) and 30 cm^{-3} (blue) density contours, including

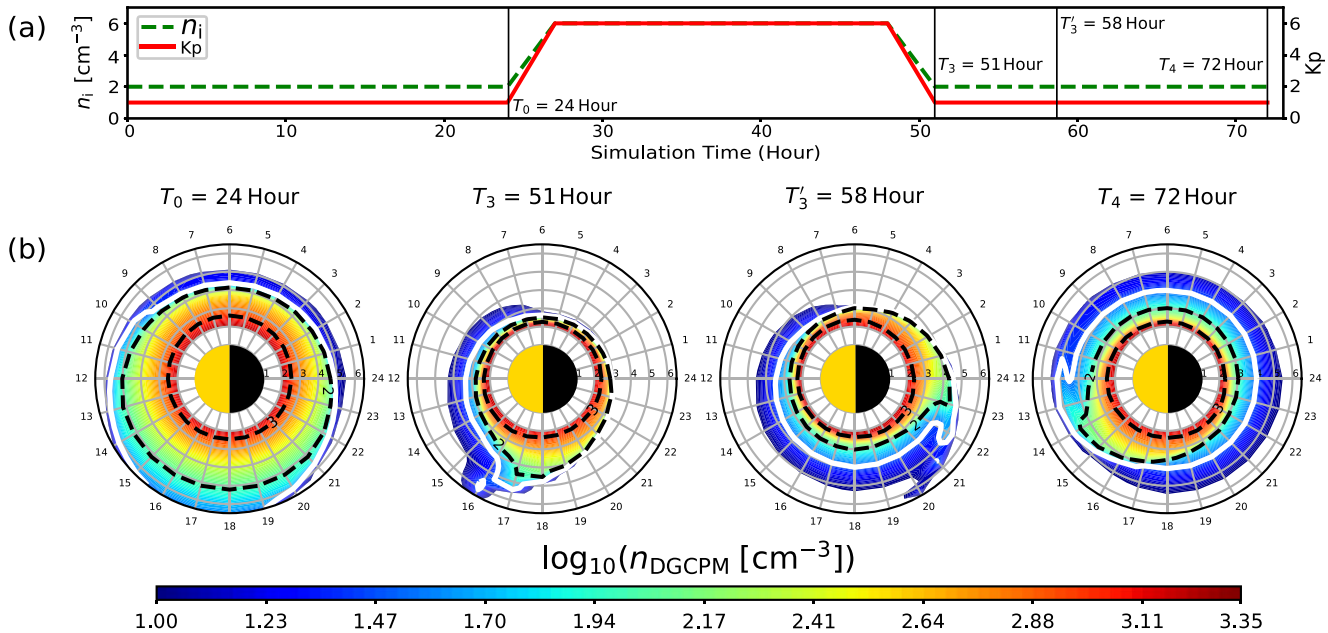

Figure 5. (a) Evolutionary tracks of the input parameters for the idealized storm simulations showing the Kp index (right *y*-axis, red line) and plasma sheet density on the nightside outer boundary (left *y*-axis, green line); (b) Plots showing the evolution of the plasmaspheric cold plasma density predicted by Ober et al. (1997) plasmasphere model (in log scale), with the white solid contour marks at constant density level of 30 cm^{-3}.

(solid) and excluding (dashed) the contribution from cold H^+ populations formed via charge exchange reactions. At the beginning of the recovery phase (T_3 = 51 hr, the second column from the left of rows (b) and (d), red solid contour versus red dashed contour), inclusion of cold H^+ produced via charge exchange reactions involving energetic O^+ into the plasmaspheric population extends the 10 cm^{-3} density contour at dawn from L = 2.75 to L = 4, and those resulting from energetic N^+ further extends it to L = 4.25. At T_3' = 58 hr, inclusion of cold H^+ produced via charge exchange reactions involving energetic O^+ into the plasmaspheric population extends the 10 cm^{-3} density contour at dawn from L = 3.25 to L = 4, and those resulting from charge exchange reactions involving energetic N^+ further extends it to L = 4.5. This expansion of the cold plasma density during the early recovery phase implies that energetic heavy ions alone are able to produce cold H^+ in amounts large enough to reshape the density distribution of the plasmasphere along with the plasmapause, especially during the early stage of the storm recovery phase. Therefore, the composition of the energetic heavy ions of the plasma sheet can affects the overall spatial extent of the plasmasphere, as shown in row (c) with (e).

The expansion of the 10 cm^{-3} plasmasphere density contour during the storm recovery phase suggests that the local density of cold H^+ produced via charge exchange can be abundant compared with the local plasmasphere density, in the L-shells just greater the red dashed contours in Figure 6. This additional source of thermal H^+ can supply a significant portion of the plasmaspheric cold population, facilitating the plasmasphere refilling rate. Figure 7 shows the ratio (in log scale) between the cold H^+ density produced by charge exchange reactions and the plasmaspheric density provided by Ober et al. (1997) model, revealing a broad region of high density ratio (~10) that lies on the nightside between L = 3 to L = 5 and MLT = 20 to MLT = 7 at the beginning of the recovery phase (T_3 = 51 hr, the second column from the left), which diminishes as the plasmasphere recovers. Comparison between the location of the 10 cm^{-3} contour at the end of the quiet phase (T_0 = 24 hr) and the start of the recovery phase (T_3 = 51 hr), highlights the presence of a plasmasphere density trough; here, the plasmaspheric cold plasma is significantly eroded during the storm main phase, and the most of the high-ratio region, including the global ratio peak, is overlapping with the density trough. Specifically, the production of cold H^+ (row (e)) can be as much as 13.6 times the local plasmasphere cold density as predicted by the DGCPM model, assuming all the heavy ions are N^+. Similarly, for the case when all the energetic heavy ions are O^+, the local production of cold H^+ by total ring current ions (row (c)) can be as much as 10 times the plasmaspheric cold density predicted by the DGCPM model. Therefore, solely considering the cold plasma supplemented from the ionosphere leads to

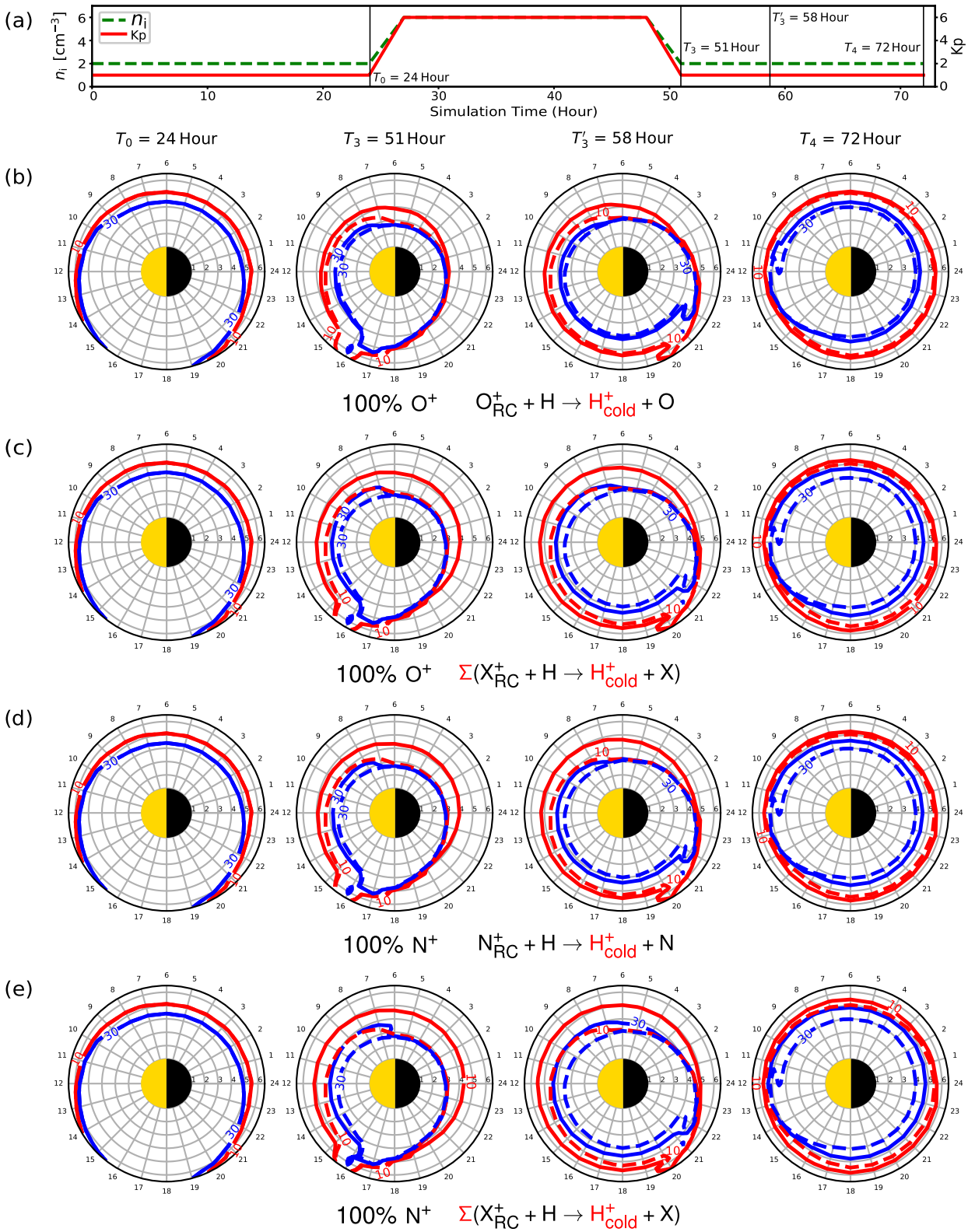

Figure 6. (a) Evolutionary tracks of the input parameters for the idealized storm simulations showing the Kp index (right *y*-axis, red line) and plasma sheet density on the nightside outer boundary (left *y*-axis, green line); (b–e) 10 cm^{-3} (red) and 30 cm^{-3} (blue) density contour levels of Ober et al. (1997) model (dashed) and the ones after considering the contribution from the charge-exchange byproduct cold H$^+$ populations (solid), using the symmetric Rairden et al. (1986) model; (b, d) Considering the byproduct cold H$^+$ that resulted from energetic heavy ions, assuming 100% O$^+$ and 100% N$^+$; (c, e) Considering the byproduct cold H$^+$ that resulted from all energetic ions, assuming 100% O$^+$ and 100% N$^+$.

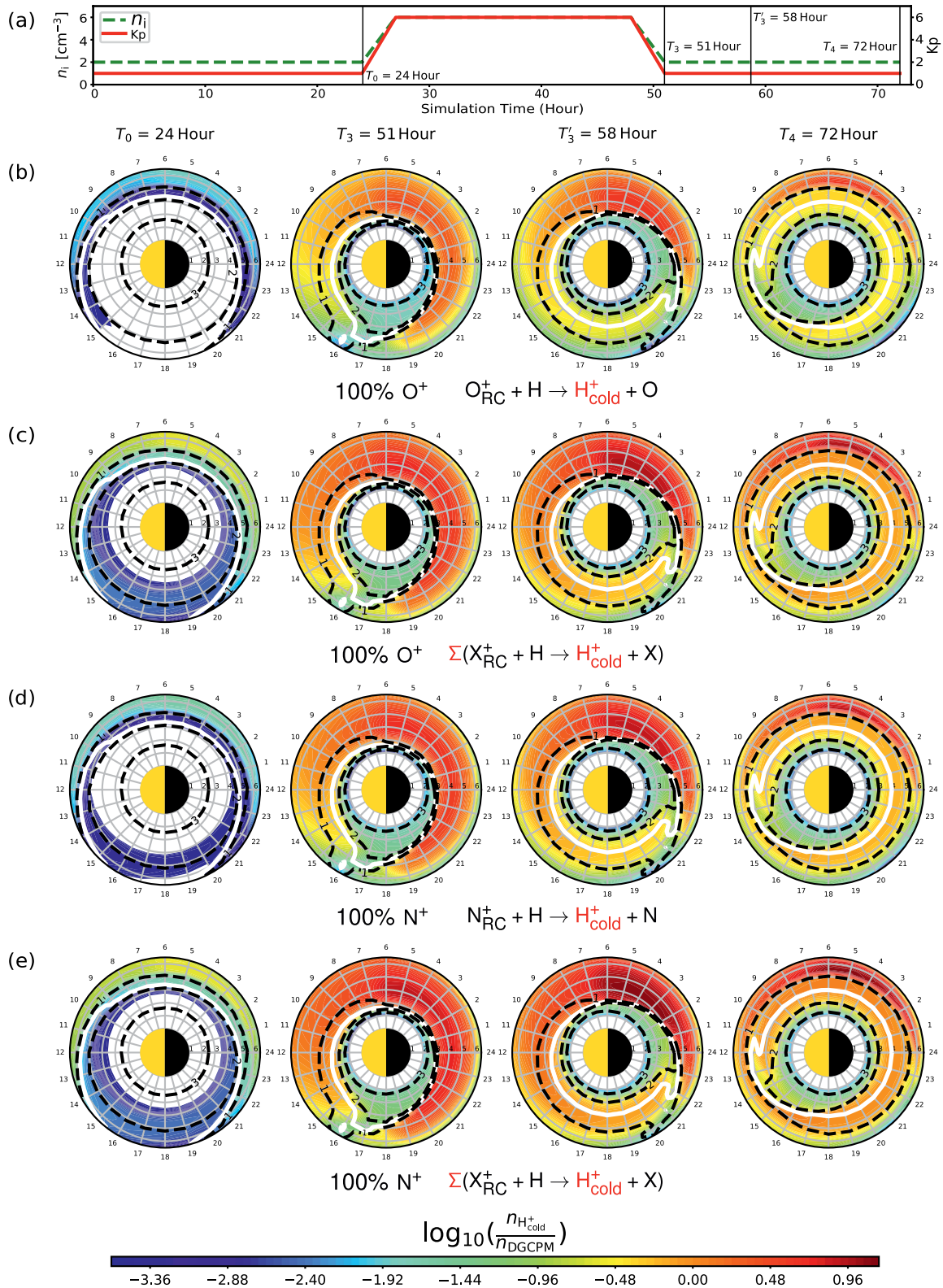

Figure 7. (a) Evolutionary tracks of the input parameters for the idealized storm simulations showing the Kp index (right *y*-axis, red line) and plasma sheet density on the nightside outer boundary (left *y*-axis, green line); (b–e) The density ratio (in log scale) between the charge-exchange byproduct cold H^+ highlighted by the red text at the bottom of each row, and the plasmaspheric cold plasma predicted by Ober et al. (1997) model. The black dashed contours represent the density levels of Ober et al. (1997) model (in log scale), and the white solid contour marks constant density level of 30 cm^{-3}. The symmetric Rairden et al. (1986) model is used.

an significant underestimation of plasmasphere density, especially in the density trough during the early stage of the recovery phase.

5. Summary and Conclusions

In this study, we quantified the role of ion composition in the plasma sheet, together with the density of exospheric neutral hydrogen in the production and transport of cold H^+ via charge exchange reactions. The simulation results show that: (a) the production and topology of the cold H^+ population are closely controlled by the composition of plasma sheet and the strength of the magnetospheric convection; (b) the density distribution of the exosphere does not play a role in shaping the peak and overall topology of the cold H^+ density distribution, which is instead shown to be primarily determined by the composition of energetic heavy ions (O^+ and N^+); (c) the cold H^+ produced via charge exchange reactions can reshape the density distribution of the plasmasphere, and has the potential to enhance the early-stage plasmaspheric refilling rate by supplying an additional source to the plasmasphere density trough; (d) The density of cold H^+ produced via charge exchange reactions can be ∼10 times greater than the local cold plasma supplied from the ionosphere in the plasmasphere density trough, therefore solely considering the supply of cold plasma from the ionosphere to the plasmasphere can lead to a significant underestimation of plasmasphere density, especially in the early recovery phase; (e) the cold H^+ deriving from charge exchange reactions involving energetic O^+ with neutral hydrogen, populate the inner L-shells, while the cold H^+ deriving from charge exchange reactions involving energetic N^+ with neutral hydrogen populate the larger L-shells.

Numerical simulations of ring current and plasmaspheric dynamics are performed under the assumption that the heavy ions supplied by the nightside plasma sheet are either O^+ or N^+. Albeit idealized, these numerical experiments reveal several important physical factors and mechanisms with profound implications regarding the generation and evolution of the cold plasma populations, including the composition of the plasma sheet, the strength and nature of the magnetospheric convection, and the interplay between the energetic ring current plasma, neutral atmosphere, and the plasmasphere. This study also infers that the cold H^+ generated via charge exchange reactions has the potential to significantly alters the local refilling of the plasmasphere during the early recovery phase.

Data Availability Statement

The HEIDI model has been included in the Space Weather Modeling Framework (SWMF), which is available for download at http://csem.engin.umich.edu/tools/swmf. The full set of simulation data is available at https://doi.org/10.6084/m9.figshare.c.5979331.v1.

Acknowledgments
Work at University of Illinois at Urbana-Champaign was performed with financial support from the NASA grant N99066ZO, NASA Grant 80NSSC20K1231, the NSF award 1664078 and NSF CAREER award 1945573. Work at University of Michigan was performed with financial support from the NASA grants 80NSSC19K0077 and 80NSSC17K0015. Joseph E. Borovsky was supported by the NSF GEM Program via grant AGS-2027569.

References

Andersson, L., Peterson, W. K., & McBryde, K. M. (2004). Dynamic coordinates for auroral ion outflow. *Journal of Geophysical Research*, *109*(A8), A08201. https://doi.org/10.1029/2004JA010424

Artemyev, A. V., Angelopoulos, V., Runov, A., & Zhang, X.-J. (2020). Ionospheric outflow during the substorm growth phase: Themis observations of oxygen ions at the plasma sheet boundary. *Journal of Geophysical Research: Space Physics*, *125*(7), e2019JA027612. https://doi.org/10.1029/2019JA027612

Bailey, J., & Gruntman, M. (2011). Experimental study of exospheric hydrogen atom distributions by Lyman-alpha detectors on the TWINS mission. *Journal of Geophysical Research (Space Physics)*, *116*(A15), A09302. https://doi.org/10.1029/2011JA016531

Bailey, J., & Gruntman, M. (2013). Experimental study of the asymmetric time varying exosphere by Lyman-alpha detectors on the TWINS mission. In *European Planetary Science Congress 2013, held 8–13 September in London, UK* (Vol. *8*, 861). Retrieved from http://meetings.copernicus.org/epsc2013id.EPSC2013-861

Borovsky, J. E., Denton, M. H., Denton, R. E., Jordanova, V. K., & Krall, J. (2013). Estimating the effects of ionospheric plasma on solar wind/magnetosphere coupling via mass loading of dayside reconnection: Ion-plasma-sheet oxygen, plasmaspheric drainage plumes, and the plasma cloak. *Journal of Geophysical Research: Space Physics*, *118*(9), 5695–5719. https://doi.org/10.1002/jgra.50527

Borovsky, J. E., Liu, J., Ilie, R., & Liemohn, M. W. (2022). Charge-exchange byproduct cold protons in the Earth's magnetosphere. *Frontiers in Astronomy and Space Sciences*, *8*, 785305. https://doi.org/10.3389/fspas.2021.785305

Brambles, O. J., Lotko, W., Damiano, P. A., Zhang, B., Wiltberger, M., & Lyon, J. (2010). Effects of causally driven cusp o+ outflow on the storm time magnetosphere-ionosphere system using a multifluid global simulation. *Journal of Geophysical Research: Space Physics*, *115*(A9), A015469. https://doi.org/10.1029/2010JA015469

Brambles, O. J., Lotko, W., Zhang, B., Wiltberger, M., Lyon, J., & Strangeway, R. J. (2011). Magnetosphere sawtooth oscillations induced by ionospheric outflow. *Science (New York, N.Y.)*, *332*(6034), 1183–1186. https://doi.org/10.1126/science.1202869

Carruthers, G. R., Page, T., & Meier, R. R. (1976). Apollo 16 Lyman alpha imagery of the hydrogen geocorona. *Journal of Geophysical Research*, *81*(10), 1664–1672. https://doi.org/10.1029/JA081i010p01664

Chamberlain, J. W. (1963). Planetary coronae and atmospheric evaporation. *Planetary and Space Science*, *11*(8), 901–960. https://doi.org/10.1016/0032-0633(63)90122-3

Chappell, C. R., Moore, T. E., & Waite, J. H., Jr. (1987). The ionosphere as a fully adequate source of plasma for the Earth's magnetosphere. *Journal of Geophysical Research*, *92*(A6), 5896–5910. https://doi.org/10.1029/JA092iA06p05896

Coley, W. R., Heelis, R. A., & Hairston, M. R. (2003). High-latitude plasma outflow as measured by the DMSP spacecraft. *Journal of Geophysical Research*, *108*(A), 1441. https://doi.org/10.1029/2003ja009890

Cornwall, J. M. (1977). On the role of charge exchange in generating unstable waves in the ring current. *Journal of Geophysical Research*, *82*(7), 1188–1196. https://doi.org/10.1029/JA082i007p01188

Dandouras, I. (2021). Ion outflow and escape in the terrestrial magnetosphere: Cluster advances. *Journal of Geophysical Research: Space Physics*, *126*(10), e2021JA029753. https://doi.org/10.1029/2021JA029753

Delzanno, G. L., Borovsky, J. E., Henderson, M. G., Resendiz Lira, P. A., Roytershteyn, V., & Welling, D. T. (2021). The impact of cold electrons and cold ions in magnetospheric physics. *Journal of Atmospheric and Solar-Terrestrial Physics*, *220*, 105599. https://doi.org/10.1016/j.jastp.2021.105599

Denton, M., & Borovsky, J. (2014). Observations and modeling of magnetic flux tube refilling of the plasmasphere at geosynchronous orbit. *Journal of Geophysical Research: Space Physics*, *119*(11), 9246–9255. https://doi.org/10.1002/2014JA020491

Fu, S. Y., Wilken, B., Zong, Q. G., & Pu, Z. Y. (2001). Ion composition variations in the inner magnetosphere: Individual and collective storm effects in 1991. *Journal of Geophysical Research*, *106*(A12), 29683–29704. https://doi.org/10.1029/2000JA900173

Genestreti, K. J., Goldstein, J., Corley, G. D., Farner, W., Kistler, L. M., Larsen, B. A., et al. (2017). Temperature of the plasmasphere from Van Allen Probes hope. *Journal of Geophysical Research: Space Physics*, *122*(1), 310–323. https://doi.org/10.1002/2016JA023047

Gershman, D. J., Avanov, L. A., Boardsen, S. A., Dorelli, J. C., Gliese, U., Barrie, A. C., et al. (2017). Spacecraft and instrument photoelectrons measured by the dual electron spectrometers on mms. *Journal of Geophysical Research: Space Physics*, *122*(11), 11548–11558. https://doi.org/10.1002/2017JA024518

Glocer, A., Tóth, G., Gombosi, T., & Welling, D. (2009). Modeling ionospheric outflows and their impact on the magnetosphere, initial results. *Journal of Geophysical Research (Space Physics)*, *114*(A13), 5216. https://doi.org/10.1029/2009JA014053

Haaland, S., Eriksson, A., André, M., Maes, L., Baddeley, L., Barakat, A., et al. (2015). Estimation of cold plasma outflow during geomagnetic storms. *Journal of Geophysical Research: Space Physics*, *120*(12), 10622–10639. https://doi.org/10.1002/2015JA021810

Hodges, R. R., Jr. (1994). Monte Carlo simulation of the terrestrial hydrogen exosphere. *Journal of Geophysical Research*, *99*(A12), 23229. https://doi.org/10.1029/94JA02183

Huddleston, M. M., Chappell, C. R., Delcourt, D. C., Moore, T. E., Giles, B. L., & Chandler, M. O. (2005). An examination of the process and magnitude of ionospheric plasma supply to the magnetosphere. *Journal of Geophysical Research*, *110*(A12), A12202. https://doi.org/10.1029/2004JA010401

Hultqvist, B. (1979). The hot ion component of the magnetospheric plasma and some relations to the electron component - observations and physical implications. *Space Science Reviews*, *23*(4), 581–675. https://doi.org/10.1007/bf00212357

Hultqvist, B. (1982). Recent progress in the understanding of the ion composition in the magnetosphere and some major question marks. *Reviews of Geophysics*, *20*(3), 589–611. https://doi.org/10.1029/RG020i003p00589

Ilie, R., & Liemohn, M. W. (2016). The outflow of ionospheric nitrogen ions: A possible tracer for the altitude-dependent transport and energization processes of ionospheric plasma. *Journal of Geophysical Research: Space Physics*, *121*(9), 9250–9255. https://doi.org/10.1002/2015ja022162

Ilie, R., Liemohn, M. W., & Toth, G. (2015). Testing the magnetotail configuration based low 2 altitude isotropic boundaries. *Journal of Geophysical Research (Space Physics)*, *120*(12), 10-557. https://doi.org/10.1002/2015JA021858

Ilie, R., Liemohn, M. W., Toth, G., & Skoug, R. M. (2012). Kinetic model of the inner magnetosphere with arbitrary magnetic field. *Journal of Geophysical Research: Space Physics*, *117*(A4), 4208. https://doi.org/10.1029/2011JA017189

Ilie, R., Skoug, R., Funsten, H., Liemohn, M., Bailey, J., & Gruntman, M. (2013). The impact of geocoronal density on ring current development. *Journal of Atmospheric and Solar-Terrestrial Physics*, *99*, 92–103. https://doi.org/10.1016/j.jastp.2012.03.010

James, M. K., Yeoman, T. K., Jones, P., Sandhu, J. K., & Goldstein, J. (2021). The scalable plasma ion composition and electron density (spiced) model for Earth's inner magnetosphere. *Journal of Geophysical Research: Space Physics*, *126*(9), e2021JA029565. https://doi.org/10.1029/2021JA029565

Kistler, L. M., Ipavich, F. M., Hamilton, D. C., Gloeckler, G., Wilken, B., Kremser, G., & Stüdemann, W. (1989). Energy spectra of the major ion species in the ring current during geomagnetic storms. *Journal of Geophysical Research*, *94*(A4), 3579–3599. https://doi.org/10.1029/JA094iA04p03579

Kistler, L. M., & Mouikis, C. G. (2016). The inner magnetosphere ion composition and local time distribution over a solar cycle. *Journal of Geophysical Research: Space Physics*, *121*(3), 2009–2032. https://doi.org/10.1002/2015ja021883

Kozyra, J. U., Liemohn, M. W., Clauer, C. R., Ridley, A. J., Thomsen, M. F., Borovsky, J. E., et al. (2002). Multistep Dst development and ring current composition changes during the 4–6 June 1991 magnetic storm. *Journal of Geophysical Research (Space Physics)*, *107*(A8), 1224. https://doi.org/10.1029/2001JA000023

Lee, J. H., Blum, L. W., & Chen, L. (2021). On the impacts of ions of ionospheric origin and their composition on magnetospheric emic waves. *Frontiers in Astronomy and Space Sciences*, *8*, 122. https://doi.org/10.3389/fspas.2021.719715

Liemohn, M. W. (2006). Introduction to special section on "Results of the National Science Foundation Geospace Environment Modeling Inner Magnetosphere/Storms Assessment Challenge". *Journal of Geophysical Research*, *111*(A11), A11S01. https://doi.org/10.1029/2006JA011970

Liemohn, M. W., & Kozyra, J. U. (2003). Lognormal form of the ring current energy content. *Journal of Atmospheric and Solar-Terrestrial Physics*, *65*(7), 871–886. https://doi.org/10.1016/S1364-6826(03)00088-9

Liemohn, M. W., & Kozyra, J. U. (2005). Testing the hypothesis that charge exchange can cause a two-phase decay. In T. I. Pulkkinen, N. A. Tsyganenko, & R. H. W. Friedel (Eds.), *The inner magnetosphere: Physics and modeling* (Vol. *155*, 211).

Liemohn, M. W., Kozyra, J. U., Jordanova, V. K., Khazanov, G. V., Thomsen, M. F., & Cayton, T. E. (1999). Analysis of early phase ring current recovery mechanisms during geomagnetic storms. *Geophysical Research Letters*, *26*(18), 2845–2848. https://doi.org/10.1029/1999GL900611

Liemohn, M. W., Ridley, A. J., Brandt, P. C., Gallagher, D. L., Kozyra, J. U., Ober, D. M., et al. (2005). Parametric analysis of nightside conductance effects on inner magnetospheric dynamics for the 17 April 2002 storm. *Journal of Geophysical Research (Space Physics)*, *110*(A9), 12. https://doi.org/10.1029/2005JA011109

Liemohn, M. W., Ridley, A. J., Gallagher, D. L., Ober, D. M., & Kozyra, J. U. (2004). Dependence of plasmaspheric morphology on the electric field description during the recovery phase of the 17 April 2002 magnetic storm. *Journal of Geophysical Research*, *109*(A3), A03209. https://doi.org/10.1029/2003JA010304

Moore, T. E., Chappell, C. R., Chandler, M. O., Craven, P. D., Giles, B. L., Pollock, C. J., et al. (1997). High-altitude observations of the polar wind. *Science*, *277*(5324), 349–351. https://doi.org/10.1126/science.277.5324.349

Mozer, F., Agapitov, O., Angelopoulos, V., Hull, A., Larson, D., Lejosne, S., & McFadden, J. (2016). Extremely field-aligned cool electrons in the dayside outer magnetosphere: Field-aligned cool electrons. *Geophysical Research Letters*, *44*(1), 51. https://doi.org/10.1002/2016GL072054
Obana, Y., Menk, F. W., & Yoshikawa, I. (2010). Plasma refilling rates for l = 2.3–3.8 flux tubes. *Journal of Geophysical Research: Space Physics*, *115*(A3), A03204. https://doi.org/10.1029/2009JA014191
Ober, D. M., Horwitz, J. L., & Gallagher, D. L. (1997). Formation of density troughs embedded in the outer plasmasphere by subauroral ion drift events. *Journal of Geophysical Research*, *102*(A7), 14595–14602. https://doi.org/10.1029/97JA01046
Orsini, S. (2004). Modeling the time-evolving plasma in the inner magnetosphere: An empirical approach. *Journal of Geophysical Research*, *109*(A11), 18391. https://doi.org/10.1029/2004ja010532
Ouellette, J. E., Brambles, O. J., Lyon, J. G., Lotko, W., & Rogers, B. N. (2013). Properties of outflow-driven sawtooth substorms. *Journal of Geophysical Research: Space Physics*, *118*(6), 3223–3232. https://doi.org/10.1002/jgra.50309
Phaneuf, R. A., Janev, R. K., & Pindzola, M. S. (1987). Collisions of carbon and oxygen ions with electrons, H, H2 and He.
Rairden, R. L., Frank, L. A., & Craven, J. D. (1986). Geocoronal imaging with dynamics explorer. *Journal of Geophysical Research*, *91*(A12), 13613–13630. https://doi.org/10.1029/JA091iA12p13613
Rapp, D., & Francis, W. E. (1962). Charge exchange between gaseous ions and atoms. *The Journal of Chemical Physics*, *37*(11), 2631–2645. https://doi.org/10.1063/1.1733066
Smith, P. H., & Bewtra, N. K. (1978). Charge exchange lifetimes for ring current ions. *Space Science Reviews*, *22*(3), 301–318. https://doi.org/10.1007/BF00239804
Sojka, J. J., & Wrenn, G. L. (1985). Refilling of geosynchronous flux tubes as observed at the equator by geos 2. *Journal of Geophysical Research*, *90*(A7), 6379–6385. https://doi.org/10.1029/JA090iA07p06379
Stern, D. P. (1975). The motion of a proton in the equatorial magnetosphere. *Journal of Geophysical Research*, *80*(4), 595–599. https://doi.org/10.1029/JA080i004p00595
Su, Y.-J., Thomsen, M. F., Borovsky, J. E., & Lawrence, D. J. (2001). A comprehensive survey of plasmasphere refilling at geosynchronous orbit. *Journal of Geophysical Research*, *106*(A11), 25615–25629. https://doi.org/10.1029/2000JA000441
Thomsen, M. F., Denton, M. H., Gary, S. P., Liu, K., & Min, K. (2017). Ring/shell ion distributions at geosynchronous orbit. *Journal of Geophysical Research: Space Physics*, *122*(1), 12. https://doi.org/10.1002/2017ja024612
Thomsen, M. F., Denton, M. H., Jordanova, V. K., Chen, L., & Thorne, R. M. (2011). Free energy to drive equatorial magnetosonic wave instability at geosynchronous orbit. *Journal of Geophysical Research: Space Physics*, *116*(A8), A08220. https://doi.org/10.1029/2011JA016644
Trung, H.-S., Liemohn, M. W., & Ilie, R. (2019). Steady state characteristics of the terrestrial geopauses. *Journal of Geophysical Research: Space Physics*, *124*(7), 5070–5081. https://doi.org/10.1029/2019JA026636
Volland, H. (1973). A semiempirical model of large-scale magnetospheric electric fields. *Journal of Geophysical Research*, *78*(1), 171–180. https://doi.org/10.1029/JA078i001p00171
Welling, D. T., André, M., Dandouras, I., Delcourt, D., Fazakerley, A., Fontaine, D., et al. (2015). The Earth: Plasma sources, Losses, and transport processes. *Space Science Reviews*, *192*(1–4), 145–208. https://doi.org/10.1007/s11214-015-0187-2
Welling, D. T., Jordanova, V. K., Glocer, A., Toth, G., Liemohn, M. W., & Weimer, D. R. (2015). The two-way relationship between ionospheric outflow and the ring current. *Journal of Geophysical Research: Space Physics*, *120*(6), 4338–4353. https://doi.org/10.1002/2015JA021231
Welling, D. T., & Ridley, A. J. (2010). Exploring sources of magnetospheric plasma using multispecies MHD. *Journal of Geophysical Research*, *115*(A), A04201. https://doi.org/10.1029/2009ja014596
Wiltberger, M., Lotko, W., Lyon, J. G., Damiano, P., & Merkin, V. (2010). Influence of cusp O+ outflow on magnetotail dynamics in a multifluid MHD model of the magnetosphere. *Journal of Geophysical Research*, *115*(1), A00J05. https://doi.org/10.1029/2010ja015579
Winglee, R. M. (2000). Mapping of ionospheric outflows into the magnetosphere for varying IMF conditions. *Journal of Atmospheric and Solar-Terrestrial Physics*, *62*(6), 527–540. https://doi.org/10.1016/s1364-6826(00)00015-8
Winglee, R. M., Chua, D., Brittnacher, M., Parks, G. K., & Lu, G. (2002). Global impact of ionospheric outflows on the dynamics of the magnetosphere and cross-polar cap potential. *Journal of Geophysical Research (Space Physics)*, *107*(A9), 1237. https://doi.org/10.1029/2001JA000214
Young, D. T., Balsiger, H., & Geiss, J. (1982). Correlations of magnetospheric ion composition with geomagnetic and solar activity. *Journal of Geophysical Research*, *87*(A11), 9077–9096. https://doi.org/10.1029/JA087iA11p09077
Yu, Y., Liemohn, M. W., Jordanova, V. K., Lemon, C., & Zhang, J. (2019). Recent advancements and remaining challenges associated with inner magnetosphere cross-energy/population interactions (IMCEPI). *Journal of Geophysical Research: Space Physics*, *124*(2), 886–897. https://doi.org/10.1029/2018JA026282
Zhao, H., Li, X., Baker, D. N., Fennell, J. F., Blake, J. B., Larsen, B. A., et al. (2015). The evolution of ring current ion energy density and energy content during geomagnetic storms based on Van Allen Probes measurements. *Journal of Geophysical Research: Space Physics*, *120*(9), 7493–7511. https://doi.org/10.1002/2015JA021533
Zoennchen, J. H., Bailey, J. J., Nass, U., Gruntman, M., Fahr, H. J., & Goldstein, J. (2011). 3-D-geocoronal hydrogen density derived from TWINS Ly-α-data. *Annales Geophysicae*, *13*(6), 1221–1228. https://doi.org/10.5194/angeo-28-1221-2010
Zoennchen, J. H., Connor, H. K., Jung, J., Nass, U., & Fahr, H. J. (2022). Terrestrial exospheric dayside h-density profile at 3–15 r_E from UVIS/HDAC and twins lyman-α data combined. *Annales Geophysicae*, *40*(3), 271–279. https://doi.org/10.5194/angeo-40-271-2022
Zoennchen, J. H., Nass, U., & Fahr, H. J. (2015). Terrestrial exospheric hydrogen density distributions under solar minimum and solar maximum conditions observed by the twins stereo mission. *Annales Geophysicae*, *33*(3), 413–426. https://doi.org/10.5194/angeo-33-413-2015

Erratum

In the originally published version of this article, variable t in equation 6 was incorrectly placed outside the opening parenthesis in two places and ϕ was used in equations 6 and 7 in four places. The two occurrences of variable t have now been moved to correctly appear after the opening parentheses. The four occurrences of ϕ have been replaced with φ. In addition, Joseph E. Borovsky and Michael W. Liemohn have been added to Author Contributions for "Writing – review & editing". This version may be considered the authoritative version of record.